ZIBELINE INTERNATIONAL™ PUBLISHING

Water Conservation and Management (WCM)

DOI: http://doi.org/10.26480/wcm.01.2026.230.242

ISSN: 2523-5664 (Print)
ISSN: 2523-5672 (Online)
CODEN: WCMABD

RESEARCH ARTICLE

EXPLAINABLE AI FOR WATER STRESS (DROUGHT) PREDICTION IN SEMI-ARID TUNISIA: SPATIOTEMPORAL SHAP INSIGHTS FROM A MULTI-MODEL BENCHMARK

Majdi Argoubi[b], Kaled Mili[a*]

[a]Department of Quantitative Methods, College of Business, King Faisal University, Al-Ahsa, 31982, Saudi Arabia.
[b]Department of Quantitative Methods, University of Sousse, Sousse, Tunisia.
****Corresponding Author Email: kmili@kfu.edu.sa***

Article History:

Received 21 February 2026
Revised 04 March 2026
Accepted 24 April 2026
Available online 12 May 2026

ABSTRACT

Agricultural drought poses an escalating threat to crop production and on-farm water management across the semi-arid Mediterranean basin, yet AI-driven spatially explicit prediction frameworks remain scarce for North African drylands. This study develops an explainable artificial intelligence (XAI) framework for agricultural drought prediction across five semi-arid governorates of central Tunisia over the 2001–2022 period. A multi-source dataset of 154,704 pixel-month observations (586 pixels at 0.05° spatial resolution) was assembled by integrating 15 predictor variables spanning meteorological, topographic, edaphic, and socioeconomic domains relevant to crop stress assessment. The drought target variable (Standardized Soil Moisture Index, SSMI) was derived exclusively from GLEAM v4.2a, while soil moisture predictors were drawn from the independent NASA POWER MERRA-2 atmospheric reanalysis to ensure methodological rigor and preclude mathematical circularity. Six machine learning models were evaluated (XGBoost, LightGBM, CatBoost, RF, BPNN, and LSTM) using a strict temporal split (training: 2001–2014; testing: 2015–2020; validation: 2021–2022) focused on an unprecedented multi-year drought episode. Results show that BPNN achieved the highest predictive performance on the test set (R^2 = 0.860, SDI = 0.626), whereas XGBoost demonstrated superior generalization during the extreme 2021–2022 validation period (R^2 = 0.696, SDI = 0.448), establishing it as the most robust architecture for drought-stress prediction under extreme climate conditions. TreeSHAP interpretability analysis identifies MERRA-2 soil moisture as the dominant predictor (26.0%), followed by temperature (14.2%), sand content (10.0%), and precipitation (8.6%), revealing that edaphic conditions strongly modulate drought severity and crop water stress in the Tunisian interior. These findings provide an operational smart decision-support tool for drought early-warning and precision irrigation planning in semi-arid agricultural regions.

KEYWORDS

Agricultural drought, Explainable AI (XAI), Earth observation, SHAP, Machine Learning, Soil Moisture, Spatiotemporal Analysis, Semi-arid regions.

1. INTRODUCTION

Over the past two decades, global climate change has intensified markedly, resulting in a sharp rise in the frequency, severity, and geographic extent of drought events worldwide (Pokhrel, 2021; AghaKouchak, 2023). Agriculture ranks among the sectors most severely affected, since prolonged water deficits reduce soil moisture availability, impair crop nutrient uptake, and directly threaten food security and rural livelihoods (Ding, 2021; Li, 2023). This problem is compounded by drought-induced water shortages that force farmers to intensify groundwater pumping, further depleting already stressed aquifers (Xi, 2022). Developing robust, accurate, and interpretable smart decision-support tools for regional agricultural drought forecasting has therefore become an urgent scientific and operational priority.

Tunisia provides a particularly acute example of this challenge. Located at the southern edge of the Mediterranean basin, the country is among the most water-stressed nations globally, with renewable freshwater resources below 450 m^3 per capita per year — well under the United Nations water scarcity threshold of 1,000 m^3 (FAO, 2020; Chenoweth, 2011). The semi-arid central regions, encompassing the governorates of Kairouan, Sidi Bou Zid, Kasserine, Gafsa, and Siliana, form the agricultural heartland of Tunisia and produce the bulk of the country's cereals, olives, and vegetables. Over the last thirty years, these areas have experienced a statistically significant increase in both the frequency and intensity of drought episodes, driven by rising temperatures, declining precipitation, and heightened evaporative demand (Tramblay, 2020; Tejedor, 2016). In severe drought years, yield losses in this zone have exceeded 30%, with profound socioeconomic impacts on smallholder farmers (Verner, 2018). This context underscores the urgent need for smart, data-driven tools capable of supporting on-farm drought management decisions.

In recent years, machine learning has demonstrated considerable potential for drought forecasting thanks to its ability to capture complex

Quick Response Code	Access this article online	
	Website: www.watconman.org	**DOI:** 10.26480/wcm.01.2026.230.242

Cite The Article: Khaled Mili, Majdi Argoubi (2026). Explainable Ai for Water Stress (Drought) Prediction in Semi-Arid Tunisia: Spatiotemporal Shap Insights from A Multi-Model Benchmark. Water Conservation and Management, 10(1): 230-242.

non-linear relationships among climatic, edaphic, and topographic variables (Abbes, 2023). Tree-based ensemble methods — including Random Forest (RF) (Li, 2021), Extreme Gradient Boosting (XGBoost) (Mardian, 2023), LightGBM (Ke, 2017), and CatBoost (Prokhorenkova, 2018) — together with deep sequential architectures such as Long Short-Term Memory networks (LSTM) (Dikshit, 2021) and Backpropagation Neural Networks (BPNN) have been widely applied. However, most comparative studies assess only two or three model families simultaneously, providing limited operational guidance for smart agricultural drought monitoring systems (Tanriverdi, 2025). Moreover, the bulk of existing research has focused on temperate or humid climates, leaving a clear evidence gap for the semi-arid Mediterranean zone (Zellou, 2023).

A fundamental limitation of machine learning models in environmental sciences is their black-box nature, which hinders physical interpretability and reduces trust among end-users (Osman, 2025). Explainable Artificial Intelligence (XAI) techniques have emerged to address this issue by revealing the internal reasoning of trained models. Among them, SHapley Additive exPlanations (SHAP) stands out for its strong theoretical foundation in cooperative game theory (Lundberg, 2017). Unlike feature importance scores from Random Forest (which do not indicate effect direction) or LIME (which suffers from high instability across runs) (Molnar, 2025), SHAP delivers consistent, direction-aware, and interaction-sensitive explanations that work with any model architecture (Dikshit, 2021). Despite these advantages, most drought-related SHAP applications have remained at the global model level, rarely exploiting its capacity for spatio-temporal disaggregation (Dikshit, 2021; Zhang, 2023).

The present study bridges these gaps through three interconnected contributions. First, we benchmark six machine learning models (XGBoost, LightGBM, CatBoost, RF, LSTM, and BPNN) for agricultural drought prediction across five semi-arid governorates of central Tunisia (2001–2022), using a large multi-source dataset of 154,704 pixel-month observations integrating 15 meteorological, edaphic, topographic, and socioeconomic predictors. The target variable (SSMI, derived from GLEAM v4.2a) is predicted using fully independent variables, eliminating any mathematical circularity. Second, we implement a spatio-temporal TreeSHAP analysis that disaggregates feature contributions by season and governorate, providing physically interpretable, spatially explicit insights directly actionable for smart drought early-warning systems. Third, we conduct a rigorous governorate-level evaluation across drought intensities, highlighting the contrasting behaviour of neural-network versus tree-based architectures under extreme climate conditions.

The remainder of the paper is organised as follows. Section 2 describes the study area and datasets. Section 3 presents the methodological framework. Section 4 reports the experimental results. Section 5 interprets the findings and their practical implications. Section 6 summarises the study and outlines directions for future research.

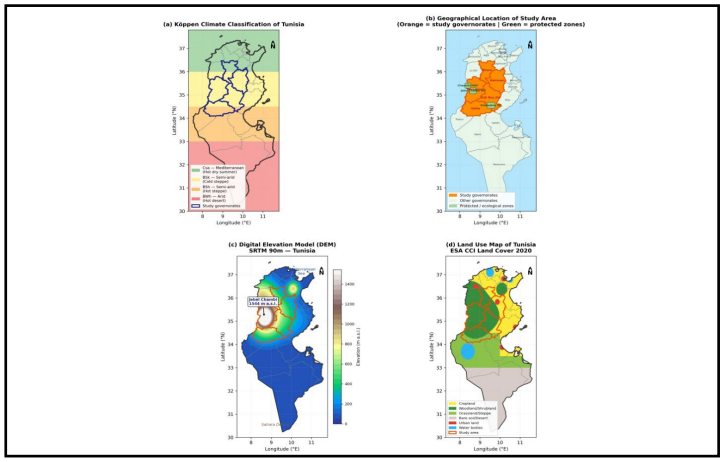

Figure 1: Study area and geographic context of the five semi-arid governorates of central Tunisia (Kairouan, Kasserine, Sidi Bou Zid, Gafsa, and Siliana). (a) Köppen climate classification of Tunisia. (b) Administrative boundaries of the five study governorates with protected areas (Jebel Chambi and Bouhedma National Parks). (c) Digital Elevation Model (SRTM 90 m) showing the topographic gradient from mountain ridges (Kasserine, Siliana) to alluvial plains (Kairouan, Sidi Bou Zid). (d) Land use classification from ESA WorldCover 2021 aggregated into four categories.

2. Regional Setting And Input Data

2.1 Geographic and Climatic Context

The present investigation focuses on five semi-arid governorates located in central Tunisia: Kairouan, Kasserine, Sidi Bou Zid, Gafsa, and Siliana, collectively spanning an area of approximately 45,000 km^2 (Figure1b). Geographically positioned between latitudes 34°N and 36.5°N and longitudes 7.5°E and 10.5°E, this territory occupies a transitional zone between the Mediterranean climate of northern Tunisia and the hyper-arid Saharan conditions of the south, straddling the BSk (cold semi-arid steppe) and BSh (hot semi-arid steppe) Köppen zones (Figure1a). Both zones are highly sensitive to precipitation variability and temperature extremes, rendering them particularly prone to agricultural drought. Over the last five decades, mean annual precipitation has declined by 15–25% while mean annual temperature has risen at approximately 0.2 °C per decade (Tramblay, 2020).

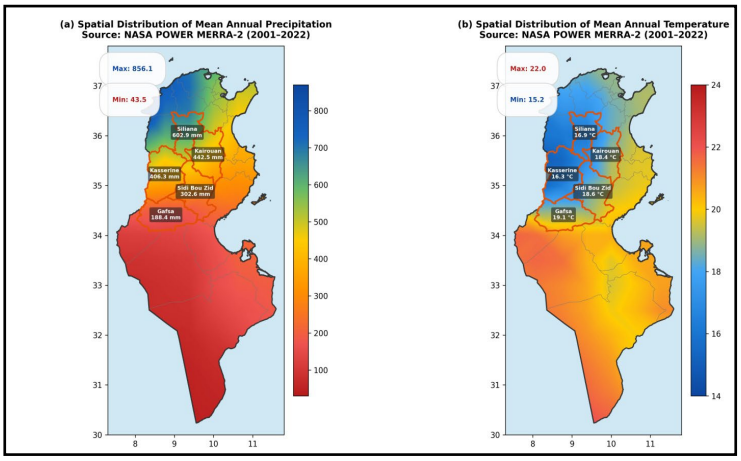

Figure 2: Spatial distribution of mean annual climate variables across the five study governorates (NASA POWER MERRA-2, 2001–2022). (a) Mean annual precipitation (mm year^{-1}), showing a clear north-to-south aridity gradient from Siliana (412 mm) to Gafsa (188 mm). (b) Mean annual temperature (°C), showing a southward warming gradient from Siliana (17.8 °C) to Gafsa (21.3 °C).

Precipitation decreases sharply from north to south across the study area (Figure2a): Siliana receives ~412 mm year^{-1} and northern Kasserine ~325 mm year^{-1}, partly due to orographic enhancement from the Jebel Chambi massif (1,544 m a.s.l.), whereas Gafsa receives only ~188 mm year^{-1}, placing it at the boundary of hyper-aridity. Mean annual temperature ranges from ~17.8°C in the mountainous western sectors to ~21.3°C in the arid lowlands of Gafsa and Sidi Bou Zid (Figure2b), in agreement with Tejedor (2017).

The five governorates form the agricultural heartland of Tunisia, with farming activities contributing approximately 18–25% of regional GDP and employing 14–20% of the active population (FAO, 2022). Main crops include durum wheat, barley, olive trees, and market garden vegetables. Agricultural land covers roughly 38–40% of the total surface area, forest and rangeland 32–33%, and bare or degraded land 25–30% (MARHP, 2023). Elevation ranges from mountain ridges exceeding 1,200 m in Kasserine to alluvial plains below 200 m across central Kairouan and Sidi Bou Zid (Figure1c). Notable drought events struck the study area in 2002, 2007, 2014, and 2021–2022, with the 2021–2022 episode proving especially critical: the Sidi Salem and El Haouareb reservoirs dropped to less than 15–20% of their storage capacity (MARHP, 2022; ONAGRI, 2023), underscoring the pressing need for reliable smart tools for agricultural drought prediction across this region.

Table 1: Basic information of the multi-source datasets used for agricultural drought prediction in semi-arid Tunisia (2001–2022).

Dataset	Resource (URL)	Resolution	Role
Target Variable			
SSMI (GLEAM v4.2a)	https://www.gleam.eu	0.05°	Target
Predictor Variables			
Surface SM (MERRA-2)	https://power.larc.nasa.gov	0.5°	Predictor
Precipitation (MERRA-2)	https://power.larc.nasa.gov	0.5°	Predictor
Temperature (MERRA-2)	https://power.larc.nasa.gov	0.5°	Predictor
Relative Humidity	https://power.larc.nasa.gov	0.5°	Predictor
Root Zone Wetness	https://power.larc.nasa.gov	0.5°	Predictor
Evapotranspiration	https://power.larc.nasa.gov	0.5°	Predictor
DEM (SRTM)	https://srtm.csi.cgiar.org	90 m	Predictor
Soil Texture (SoilGrids)	https://data.isric.org	250 m	Predictor
PAWC (SoilGrids)	https://data.isric.org	250 m	Predictor
Population Density	https://www.worldpop.org	100 m	Predictor
Land Use (ESA)	https://esa-worldcover.org	10 m	Predictor

2.2 Data Sources and Variable Selection

Selecting appropriate predictor variables constitutes a critical step in developing reliable agricultural drought forecasting models, as agricultural drought emerges from the complex interplay of numerous biophysical and anthropogenic drivers, including topographic setting, precipitation, air temperature, soil moisture dynamics, soil texture, plant-available water, land cover, and human pressures. Drawing upon a suite of globally and regionally accessible datasets, the present study incorporated 15 predictor variables distributed across five thematic categories: meteorological conditions, soil moisture, topographic attributes, soil physical properties, and socioeconomic factors. The retained predictors include surface soil moisture (SM), precipitation (PRECTOTCORR), mean air temperature (T2M), root-zone soil wetness (GWETROOT), relative humidity (RH2M), evapotranspiration (EVPTRNS), elevation, slope, topographic wetness index (TWI), clay content, sand content, plant available water capacity (PAWC), soil depth, land use, and population density. Full information on data sources, native spatial resolutions, and geographic coverage is provided in Table 1. Prior to any analysis, all input datasets were harmonised to a common spatial resolution of 0.05° (approximately 5 km) via bilinear interpolation, and all subsequent computations were performed at this unified resolution over the entire 2001–2022 study period.

Table 2: SSMI drought classification scheme adopted in this study, following McKee et al. (1993).

SSMI range	Category	Color code
≥ +1.5	Extremely humid	Dark blue
+0.5 to +1.5	Moderately humid	Light blue
−0.5 to +0.5	Near normal	White/grey
−1.0 to −0.5	Mild drought	Light yellow
−1.5 to −1.0	Moderate drought	Orange
−2.0 to −1.5	Severe drought	Red
< −2.0	Extreme drought	Dark red

2.2.1 Soil Moisture Data and Drought Target Variable (SSMI)

Monthly surface soil moisture estimates were obtained from the Global Land Evaporation Amsterdam Model version 4.2a (GLEAM v4.2a), a globally gridded dataset that provides daily values of terrestrial evaporation and root-zone soil moisture at a native spatial resolution of 0.05° (Miralles, 2025; Miralles, 2011). Monthly mean surface soil moisture values were extracted for the 586 pixels covering the five study governorates over the full 1980–2022 period, resulting in a total of 272,712 pixel-month records. These data were used exclusively to derive the drought target variable (SSMI). Importantly, GLEAM-derived soil moisture was deliberately excluded from the pool of predictor variables supplied to the machine learning models.

Antecedent soil water availability was instead represented in the predictor set by the root-zone soil wetness fraction (GWETROOT, dimensionless) and surface soil moisture (SM, m^3 m^{-3}) from NASA POWER MERRA-2, an independent atmospheric reanalysis product at 0.5° spatial resolution. This design ensures complete source independence between the drought target and its predictors, precluding any mathematical circularity in model training.

The drought target variable is the Standardized Soil Moisture Index (SSMI), computed from GLEAM v4.2a following AghaKouchak (2014):

$$SSMI\_(i,m) = (SM\_(i,m)\text{^}GLEAM - \mu\_(i,m)\text{^}ref) / \sigma\_(i,m)\text{^}ref \quad (1)$$

where SM_(i,m)^GLEAM denotes the GLEAM surface soil moisture at pixel i for calendar month m, and μ_(i,m)^ref and σ_(i,m)^ref are the long-term mean and standard deviation computed over the WMO reference period 1980–2010 at each pixel independently. The resulting SSMI ranges from −3 (extreme drought) to +3 (extreme wet), with negative values indicating below-normal soil moisture conditions. The classification scheme follows McKee (1993) and is reported in Table 2. Over the 2001–2022 study period, the mean SSMI across the five governorates was −0.106, indicating a persistent mild drought tendency consistent with documented regional aridification (Tramblay, 2020).

2.2.2 Terrain Elevation

Topographic setting exerts a major control on both precipitation distribution and temperature regimes across the study area (Francis, 2024). Elevation data were obtained from the Shuttle Radar Topography Mission (SRTM) digital elevation model at a native spatial resolution of 90 m (https://srtm.csi.cgiar.org), extensively validated across the MENA region (Gorokhovich, 2006; Purinton, 2021). As illustrated in Figure1c, the highest point is Jebel Chambi (1,544 m a.s.l.) in Kasserine, while the lowest elevations correspond to the alluvial plains of central Kairouan and Sidi Bou Zid (~200 m a.s.l.). Elevation values range from −22 m to 1,334 m, with a mean of 460 m.

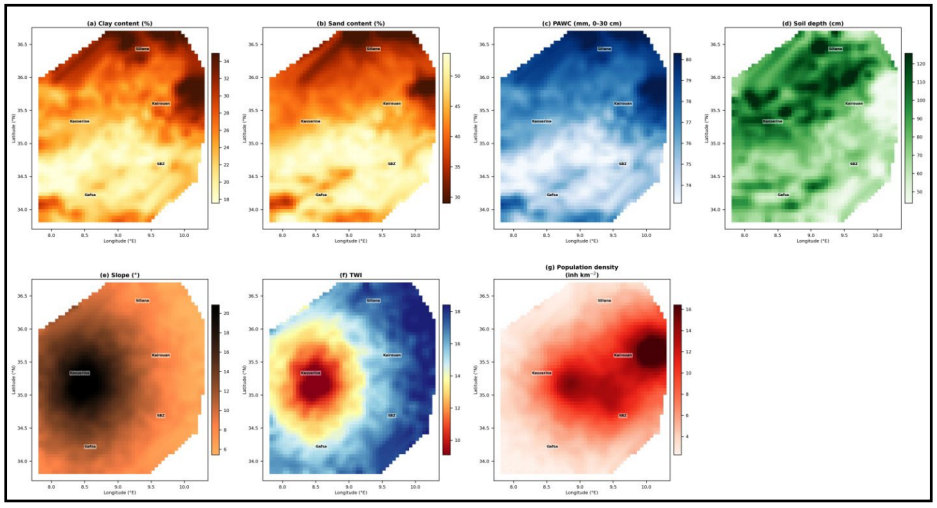

Figure 3: Spatial distribution of topographic, soil, and socioeconomic predictor variables across the five study governorates. (a) Clay content (%, SoilGrids v2.0, 0–5 cm depth). (b) Sand content (%, SoilGrids v2.0, 0–5 cm depth). (c) Plant Available Water Capacity (PAWC, mm, 0–30 cm). (d) Soil depth (cm). (e) Slope (degrees, derived from SRTM DEM). (f) Topographic Wetness Index (TWI). (g) Population density (inhabitants km^{-2}, WorldPop 2020).

2.2.3 Terrain Slope

Slope gradient is a key control on the capacity of soils to retain water following rainfall events. Gentle terrain promotes prolonged surface water infiltration and enhanced soil water storage, whereas steep gradients accelerate surface runoff and limit soil moisture recharge (Borselli, 2010; Ries, 2017). In the semi-arid setting of central Tunisia, where rainfall is frequently short-lived and convective in character, slope constitutes a critical determinant of effective water availability for crops. Slope values were derived from the SRTM DEM using the Google Earth Engine ee.Terrain.slope() function and are illustrated in Figure3e.

2.2.4 Topographic Wetness Index (TWI)

The Topographic Wetness Index (TWI) is an established indicator of surface wetness and soil moisture accumulation widely employed in hydrological investigations. It is computed as (Beven, 1979; Sorensen, 2006):

$$TWI = \ln(A / \tan B) \quad (2)$$

where A is the cumulative upslope drainage area per unit contour length (m^2 m^{-1}), and B is the local slope gradient in radians. In semi-arid environments, TWI is especially informative for delineating topographic depressions where soil moisture tends to concentrate following precipitation events, directly influencing crop water availability. TWI values were computed from the SRTM-derived slope within Google Earth Engine and are displayed in Figure 3f.

2.2.5 Physico-Chemical Soil Characterization

The capacity for moisture retention, which fundamentally dictates water availability for crops during prolonged dry spells, is primarily contingent upon soil texture and profile depth (Jabro, 2008). Augmented clay fractions, reduced sand concentrations, and greater soil thickness are systematically linked to enhanced hydraulic retention potential (Guo, 2022; Zhang, 2021). High-resolution data (250 m) for clay content, sand content, and soil depth were acquired from the ISRIC SoilGrids v2.0 repository validated across Mediterranean and North African bioclimatic zones (Poggio, 2021; Bahri, 2022). Clay concentrations range from 13.3% to 51.6% and sand content from 7.4% to 66.5%, delineating a sharp latitudinal gradient from clay-rich northern substrates to sand-dominated southern profiles. The spatial distribution of these variables, alongside PAWC and soil depth, is illustrated in Figure 3a–d.

2.2.6 Plant Available Water Capacity (PAWC)

Plant Available Water Capacity (PAWC) quantifies the volume of water that a soil can store and supply to plants between field capacity and permanent wilting point, directly reflecting the buffering capacity of the soil against short-term precipitation deficits (Romano, 2022). Within the study area, PAWC values are notably low in the sandy soils of Sidi Bou Zid and Gafsa, amplifying drought sensitivity in these governorates. PAWC was estimated using the pedotransfer functions of Saxton (2006):

$\theta_{FC} = f(\text{sand, clay, OM})$

$\theta_{WP} = g(\text{clay, sand, OM})$

$$PAWC = (\theta_{FC} - \theta_{WP}) \times 300 \quad [\text{mm for 0–30 cm}] \quad (3)$$

where θ_{FC} and θ_{WP} denote volumetric water contents at field capacity (−33 kPa) and wilting point (−1500 kPa) respectively, and organic matter content (OM) was set to 2%. PAWC values range from 70.8 to 82.9 mm for the 0–30 cm soil layer in Figure 3c.

2.2.7 Atmospheric Forcing Variables

Five meteorological predictor variables were extracted from the NASA POWER database based on the MERRA-2 reanalysis product (https://power.larc.nasa.gov) at 0.5° × 0.625° spatial resolution for 2001–2022 using the monthly aggregation endpoint: (1) bias-corrected total precipitation (PRECTOTCORR, mm day^{-1}), (2) air temperature at 2 m height (T2M, °C), (3) root zone soil wetness (GWETROOT, dimensionless), (4) relative humidity at 2 m (RH2M, %), and (5) evapotranspiration (EVPTRNS, mm day^{-1}). These variables capture the principal atmospheric drivers of agricultural drought at monthly timescales: water input, thermal demand, atmospheric moisture, land-surface water availability, and water flux. Monthly values were retrieved for 64 grid points covering the study domain and subsequently interpolated onto the common 0.05° grid via bilinear interpolation. NASA POWER MERRA-2 data are widely adopted as reliable inputs for drought and agroclimatological modelling across Mediterranean and North African regions (Muñoz-Sabater, 2021; Ouassanouan, 2025).

2.2.8 Human Pressure: Population Density

In semi-arid regions, growing population pressure frequently drives the overexploitation of water resources through unsustainable groundwater extraction and the expansion of irrigated agriculture, compounding drought vulnerability (Fitton, 2019). Within the study area, this pressure is particularly pronounced in Sidi Bou Zid and Kairouan, where agricultural intensification has led to significant overexploitation of the Zeramdine and Merguellil aquifers (MARHP, 2023). Population density data were sourced from the WorldPop Global dataset for 2020 at 100 m resolution, extracted via Google Earth Engine (Lloyd, 2017; Gorelick, 2017). Values range from near zero to 51 inhabitants km^{-2}, with peak concentrations in the urban centers of Kairouan and Kasserine as shown in Figure 3g.

2.2.9 Land Cover Classification

Land cover type exerts a strong influence on local water balances through its contrasting effects on evapotranspiration, surface infiltration, and runoff generation (Strohbach, 2019; Nadal-Romero, 2025). Land cover data were obtained from the ESA WorldCover 2021 product at 10 m resolution, extracted via Google Earth Engine and resampled to 0.05°. The original ESA classes were consolidated into four broad categories: cropland (17.9%), grassland and steppe (8.5%), bare soil and desert (65.6%), and urban land (0.2%), with water bodies and other minor classes accounting for the remaining 7.8% (Figure1d). The ESA WorldCover product has been extensively validated across North Africa (Xu, 2024; Zanaga, 2022).

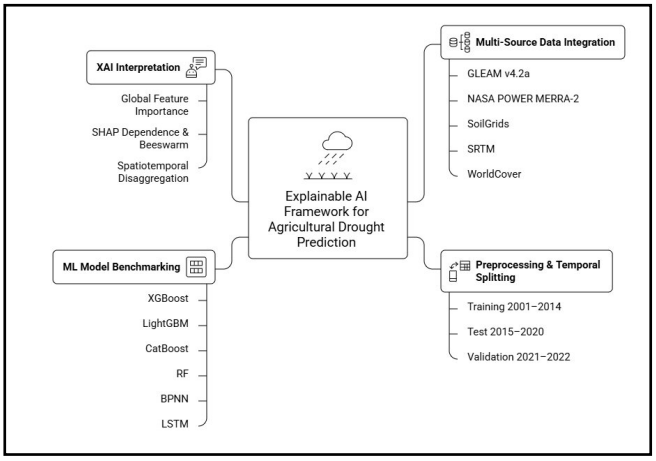

Figure 4: Methodological flowchart of the study. The framework comprises four sequential steps: (1) SSMI computation from GLEAM v4.2a soil moisture data; (2) multi-source dataset assembly (15 predictor variables, 154,704 pixel-month observations); (3) training and evaluation of six machine learning models using temporal split (2001–2014 training, 2015–2020 test, 2021–2022 validation); and (4) TreeSHAP interpretability analysis at global, feature-effect, and spatiotemporal scales.

3. Methodological Framework

The conceptual workflow of this research, as delineated in Figure4, is organized into four primary analytical phases: (a) characterization of agricultural drought dynamics across five semi-arid governorates for 2001–2022 using the Standardized Soil Moisture Index (SSMI); (b) conFigureuration and training of six machine learning architectures — XGBoost, LightGBM, CatBoost, Random Forest (RF), BPNN, and LSTM — with 15 predictors spanning meteorological, edaphic, topographic, and socioeconomic domains; (c) comparative evaluation of model performance using four statistical metrics; and (d) implementation of TreeSHAP on the optimal model to quantify feature importance across global and spatiotemporal scales. Detailed descriptions are provided in the subsequent subsections.

3.1 Quantification of Agricultural Drought Severity

Deficits in soil moisture serve as a primary physical proxy for agricultural drought, with the Standardized Soil Moisture Index (SSMI) gaining prominence as a robust metric for quantifying moisture-induced crop stress (Hao, 2013; Sun, 2022). The efficacy of the SSMI has been extensively documented across diverse climatic regimes; notably, Sun (2022) demonstrated its superior sensitivity relative to the Standardized Precipitation Evapotranspiration Index (SPEI) and the Palmer Drought Severity Index (PDSI) for long-term drought monitoring. The index has also proven effective for assessing moisture constraints in dryland and semi-arid agroecosystems (Palagiri, 2024). Given the heterogeneous landscape of the study area — characterized by a mosaic of croplands, steppes, and degraded rangelands — the SSMI was adopted to capture the drought signal across the five governorates, derived from monthly surface soil moisture estimates from GLEAM v4.2a, with drought classification following Table 2.

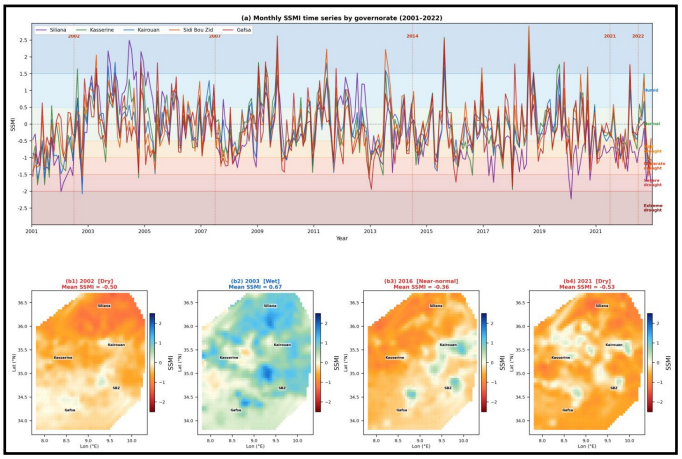

Figure 5: Spatiotemporal distribution of the Standardized Soil Moisture Index (SSMI) across the five study governorates, 2001–2022 (GLEAM v4.2a, 0.05° resolution). (a) Monthly SSMI time series averaged by governorate, with drought categories indicated by color bands (dark red: extreme/severe drought; orange: moderate drought; yellow: mild drought). (b) Spatial distribution of mean annual SSMI for selected drought years (2002, 2021) and wet years (2003).

The GLEAM v4.2a surface soil moisture product synthesizes satellite-derived observations — including passive microwave and optical data — with climate reanalysis products to generate spatially consistent soil moisture fields at 0.05° resolution (Miralles, 2025; Hulsman, 2023). Spanning 1980–2022, GLEAM v4.2a provides a high-fidelity dataset suitable for drought surveillance in data-limited semi-arid regions (Miralles, 2025; Koppa, 2022). The temporal trajectory of edaphic drought conditions from 2001 to 2022 is presented in Figure5, identifying multiple acute drought phases with peak intensities in 2002, 2007, 2014, and 2021–2022.

Table 3: Summary statistics of the 15 predictor features in the assembled dataset (154,704 pixel- month observations, 2001–2022).

Feature	Domain	Unit	Min	Max
Soil Moisture (SM)	Soil moisture	$m^3\ m^{-3}$	0.04	0.35
PRECTOTCORR	Meteorological	mm day^{-1}	0.00	8.72
T2M	Meteorological	°C	3.1	36.8
GWETROOT	Meteorological	—	0.01	0.99
RH2M	Meteorological	%	18.3	85.4
EVPTRNS	Meteorological	mm day^{-1}	0.00	5.21

Table 3(Cont.): Summary statistics of the 15 predictor features in the assembled dataset (154,704 pixel- month observations, 2001–2022).				
Elevation	Topographic	m	−22	1334
Slope	Topographic	degrees	0.0	38.7
TWI	Topographic	—	3.1	18.6
Clay content	Soil properties	%	13.3	51.6
Sand content	Soil properties	%	7.4	66.5
PAWC	Soil properties	mm	70.8	82.9
Soil depth	Soil properties	cm	28	200
Land use	Socioeconomic	class (1–4)	1	4
Population density	Socioeconomic	inh km^{-2}	0	51

Target variable: SSMI (mean = −0.106, std = 0.962, range: [−3.12, +3.08])

3.2 Dataset Assembly and Temporal Partitioning

The machine learning dataset was constructed by integrating the five multi-source data categories described in Section 2 at 0.05° spatial resolution, resulting in 154,704 pixel-month observations across 586 study pixels and 264 monthly time steps (January 2001 – December 2022). Each observation comprises 15 predictor features and one target variable (SSMI), spanning five thematic domains: meteorological variables (PRECTOTCORR, T2M, GWETROOT, RH2M, EVPTRNS), independent soil moisture from MERRA-2 (SM), topographic variables (elevation, slope, TWI), soil properties (clay, sand, PAWC, soil depth), and socioeconomic variables (land use, population density). Descriptive statistics are reported in Table 3.

The dataset was divided into three non-overlapping subsets via temporal splitting to prevent data leakage: a training set (2001–2014, 98,448 observations, 63.6%) used to optimize all model parameters; a test set (2015–2020, 42,192 observations, 27.3%) used to assess out-of-sample predictive performance; and a validation set (2021–2022, 14,064 observations, 9.1%) reserved for final independent evaluation over the most recent drought episode. A temporal splitting approach was favored over random cross-validation to preserve the chronological ordering of observations and eliminate the risk of inflated performance estimates from future information leakage (Roberts, 2017). All six models were fitted exclusively on the 2001–2014 training subset.

3.3 Machine Learning Architectures

3.3.1 XGBoost

XGBoost (eXtreme Gradient Boosting) is an advanced implementation of the Gradient Boosting Decision Tree (GBDT) ensemble that minimizes a differentiable loss function via gradient descent, employing a second-order Taylor expansion of the objective function and a regularization component (Ω) to penalize architectural complexity and mitigate overfitting (Chen, 2016). Cache-aware block structures and parallelized tree synthesis enhance computational efficiency on large datasets. XGBoost has demonstrated high predictive fidelity across diverse hydro-climatic forecasting contexts (Zhang, 2023; Ekmekcioglu, 2023). Hyperparameters were set as follows: n_estimators = 500, max_depth = 6, learning_rate = 0.05, subsample = 0.8, colsample_bytree = 0.8, reg_alpha = 0.1, reg_lambda = 1.0, with early stopping at 50-round patience.

3.3.2 LightGBM

LightGBM employs two transformative techniques: Gradient-based One-Side Sampling (GOSS), which accelerates convergence by prioritizing instances with higher gradient contributions, and Exclusive Feature Bundling (EFB) (Ke, 2017). Its leaf-wise (best-first) growth strategy yields deeper tree structures with reduced memory overhead, making it highly effective for high-dimensional climatological datasets (Zhang, 2023; Li, 2023). ConFigureuration: n_estimators = 500, max_depth = 6, learning_rate = 0.05, subsample = 0.8, colsample_bytree = 0.8, reg_alpha = 0.1, reg_lambda = 1.0, with 50-round early stopping.

3.3.3 CatBoost

CatBoost addresses prediction shift and gradient bias through ordered boosting and symmetric (oblivious) decision trees, using a permutation-based approach to estimate leaf values from independent data subsets (Prokhorenkova, 2018). Its robustness to hyperparameter variations makes it well-suited for complex environmental modelling (Elmotawakkil, 2025; Tanriverdi, 2025). Parameters: iterations = 500, depth = 6, learning_rate = 0.05, l2_leaf_reg = 3, with 50-round early stopping.

3.3.4 Random Forest (RF)

Random Forest aggregates multiple uncorrelated decision trees through bootstrap aggregation (bagging) and random feature sub-sampling at each node split, fostering ensemble diversity and enhancing generalization to unseen data (Breiman, 2001). RF remains a benchmark for integrating multi-source geospatial data in drought surveillance (Lotfirad, 2022). Parameters: n_estimators = 200, max_depth = 15, min_samples_leaf = 5. Training was performed on a randomized subset of 80,000 observations to accommodate memory constraints while preserving statistical representativeness.

3.3.5 BPNN

The Backpropagation Neural Network (BPNN) is a feedforward multi-layer perceptron trained via the generalized delta rule where residuals are back-propagated to refine synaptic weights via gradient descent (Liu, 2022; Pedregosa, 2011). Implemented via scikit-learn, the BPNN featured three hidden layers (128, 64, and 32 neurons) with ReLU activation and learning rate of 0.001. Training was capped at 300 iterations with 10-round early stopping on a 10% internal validation set. Feature scaling used StandardScaler to ensure zero-mean and unit-variance distribution.

3.3.6 LSTM

The Long Short-Term Memory (LSTM) network mitigates the vanishing gradient phenomenon through an internal cell state regulated by input, forget, and output gates, making it well-suited for capturing non-linear temporal dependencies in agricultural drought and soil moisture dynamics (Hochreiter, 1997; Dikshit, 2021). The architecture comprised a 64-unit recurrent layer, a dropout layer (rate = 0.2), and a 32-neuron dense layer with ReLU activation, followed by a linear output unit. Training used the Adam optimizer with MSE loss over 50 epochs (batch size = 256) on 80,000 observations with prior feature standardization.

3.4 Statistical Performance Evaluation

Predictive accuracy was quantified using four complementary indices: the Skill Difference Index (SDI), the Coefficient of Determination (R^2), the Root Mean Square Error (RMSE), and the Mean Absolute Error (MAE).

The SDI evaluates the concordance between predicted and observed drought intensities (Moriasi, 2007):

$$SDI = 1 - \sqrt{(MSE / Var(y))} \quad (4)$$

where MSE is the mean squared error between estimated and observed SSMI values, and Var(y) is the variance of observed SSMI. SDI ranges from −∞ to 1, with values approaching unity indicating high fidelity in replicating drought patterns. The remaining metrics are:

$$R^2 = 1 - [\Sigma_{i=1}^{n} (y_i - \hat{y}_i)^2] / [\Sigma_{i=1}^{n} (y_i - \bar{y})^2] \quad (5)$$

$$RMSE = \sqrt{(1/n \cdot \Sigma_{i=1}^{n} (y_i - \hat{y}_i)^2)} \quad (6)$$

$$MAE = (1/n) \cdot \Sigma_{i=1}^{n} |y_i - \hat{y}_i| \quad (7)$$

where $\hat{y}_i$ and y_i denote predicted and observed SSMI values for instance i, $\bar{y}$ is the observed mean, and n is the total sample size (Choubin, 2020; Moriasi, 2007).

3.5 Model Interpretability via TreeSHAP Analysis

To enhance the physical interpretability of the machine learning ensemble, this study employs the SHAP (SHapley Additive exPlanations) framework, rooted in cooperative game theory (Lundberg, 2017; Molnar, 2025). Each predictor i is assigned a Shapley value (φ_i) that decomposes the aggregate model prediction into additive contributions of individual features, revealing both directional influence and relative magnitude on the forecasted SSMI. Positive φ_i values denote a shift toward wetter

conditions, while negative values indicate contributions toward drought intensification.

The attribution for feature i is:

$$\varphi_i = \Sigma_{S \subseteq N \setminus \{i\}} [(|S|! \cdot (m - |S| - 1)!) / m!] \cdot [f(S \cup \{i\}) - f(S)] \quad (8)$$

where N is the complete feature set, m = |N| = 15, S is a subset excluding feature i, and [f(S ∪ {i}) − f(S)] captures the marginal impact of including variable i. The additive completeness property ensures:

$$f(x) = \varphi_0 + \Sigma_{i=1}^{M} \varphi_i \quad (9)$$

where φ_0 is the baseline expectation (mean training prediction) and M = 15.

The TreeSHAP explainer (Lundberg, 2020) was applied to the XGBoost model, selected for its robust generalization on both the test set (R^2 = 0.817) and the independent 2021–2022 validation set (R^2 = 0.696). TreeSHAP exploits the internal structure of decision trees for exact Shapley value computation in polynomial time (TLD^2) (Lundberg, 2020).

For computational feasibility, SHAP values were derived from a representative sample of 2,000 observations (seed = 42). Analysis was conducted at three hierarchical levels: (i) global feature importance, based on mean absolute SHAP values ($|\varphi_i|$); (ii) feature-response dynamics, using beeswarm and dependence plots for key predictors (SM, T2M, sand content, PRECTOTCORR); and (iii) spatiotemporal attribution, mapping and seasonal disaggregation of φ_i values to identify regional and cyclic drought drivers.

3.6 Software Environment and Data Reproducibility

The computational workflow was executed using Python 3.11. Model development leveraged xgboost, lightgbm, catboost, and scikit-learn, while the LSTM was implemented via TensorFlow and Keras (Chen et. al, 2016). Interpretability relied on the shap library. Spatial data processing used rasterio, geopandas, and matplotlib. The complete source code is publicly available at https://github.com/ARGOUBI25/drought-prediction-tunisia.

Table 4: Predictive performance of the six machine learning models on the test set (2015–2020) and the independent validation set (2021–2022). Best values in bold.

	Test set (2015–2020)				Validation set (2021–2022)			
Model	**SDI**	**R^2**	**RMSE**	**MAE**	**SDI**	**R^2**	**RMSE**	**MAE**
BPNN	**0.626**	**0.860**	**0.363**	**0.263**	0.413	0.655	0.477	0.342
XGBoost	0.572	0.817	0.415	0.301	**0.448**	**0.696**	**0.448**	**0.336**
LightGBM	0.561	0.807	0.427	0.313	0.437	0.683	0.458	0.345
LSTM	0.541	0.790	0.445	0.329	0.423	0.667	0.469	0.361
CatBoost	0.506	0.756	0.480	0.358	0.409	0.651	0.480	0.370
RF	0.435	0.681	0.548	0.392	0.361	0.591	0.520	0.392

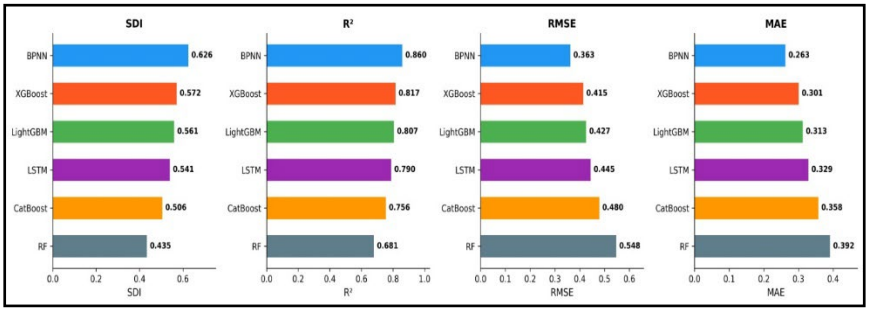

Figure 6: Comparative performance of the six machine learning models on the test set (2015–2020), evaluated using four metrics: SDI, R^2, RMSE, and MAE. Models are ranked by SDI in descending order. BPNN achieves the highest overall performance (SDI = 0.626, R^2 = 0.860), followed by XGBoost (R^2 = 0.817) and LightGBM (R^2 = 0.807).

4. Results

4.1 Comparative Model Performance Analysis

The predictive performance of the six machine learning architectures — XGBoost, LightGBM, CatBoost, RF, BPNN, and LSTM — was assessed using SDI, R^2, RMSE, and MAE across the test set (2015–2020) and the independent validation set (2021–2022). Results are illustrated in Figure6 and summarized in Table 4.

On the test period (2015–2020), BPNN demonstrated superior predictive accuracy (R^2 = 0.860, SDI = 0.626, RMSE = 0.363, MAE = 0.263), followed by XGBoost (R^2 = 0.817, SDI = 0.572), LightGBM (R^2 = 0.807), LSTM (R^2 = 0.790), CatBoost (R^2 = 0.756), and RF (R^2 = 0.681).

On the independent validation set (2021–2022), XGBoost maintained the highest robustness (R^2 = 0.696, SDI = 0.448, RMSE = 0.448), marginally outperforming LSTM (R^2 = 0.667) and BPNN (R^2 = 0.655). A general decrease in statistical skill was observed across all models during this period, with a regional mean SSMI of −0.406 and 48.8% of observations reflecting drought conditions.

Table 5: XGBoost model performance by governorate on the validation set (2021–2022).

Governorate	n	SDI	R^2	RMSE
Sidi Bou Zid	1,584	**0.548**	**0.796**	**0.406**
Kasserine	3,888	0.502	0.752	0.414
Gafsa	3,312	0.448	0.696	0.435
Kairouan	3,744	0.449	0.697	0.437
Siliana	1,536	−0.105	−0.221	0.603

The governorate-specific validation metrics show in table 5 reveal substantial spatial variability in model reliability. Sidi Bou Zid exhibited the highest XGBoost fidelity (R^2 = 0.796, SDI = 0.548), followed by Kasserine (R^2 = 0.752) and Gafsa (R^2 = 0.696). Predictive skill deteriorated

significantly in Siliana, where tree-based models yielded negative SDI values (XGBoost: R^2 = −0.221, SDI = −0.105), while BPNN achieved the best relative SDI (−0.038) and LSTM was the sole architecture to maintain a positive R^2 (0.104).

4.2 Spatiotemporal Prediction Analysis

The predictive framework was deployed to estimate monthly SSMI values across the five governorates for the independent validation window (2021–2022), characterized by a mean regional observed SSMI of −0.406. Statistical breakdown of observed conditions reveals 27.7% of pixels under mild drought (−1.0 to −0.5), 16.0% under moderate drought (−1.5 to −1.0), 4.6% under severe drought (−2.0 to −1.5), and 0.9% reaching the extreme drought threshold (≤ −2.0).

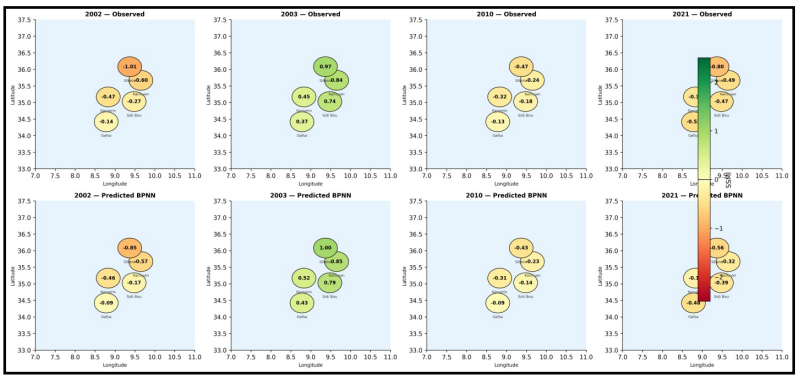

Figure 7: Spatial distribution of observed (GLEAM v4.2a) and BPNN-predicted SSMI across the five study governorates for selected years: 2002 (dry), 2003 (wet), 2010 (near-normal), and 2021 (dry). Annual mean SSMI values are shown for each governorate centroid. Positive values (green) indicate above-normal soil moisture; negative values (red) indicate drought conditions.

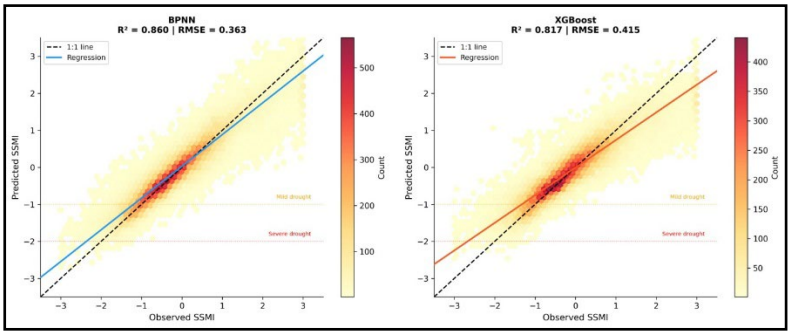

Figure 8: Probability density scatter plots of observed vs. predicted SSMI for BPNN (best test-set performance, R^2 = 0.860) and XGBoost (best validation performance, R^2 = 0.696), evaluated over the test period (2015–2020). The 1:1 line (dashed black) and the linear regression line (solid) are shown. Horizontal dotted lines indicate drought classification thresholds (orange: mild drought at SSMI = −1.0; red: severe drought at SSMI = −2.0). The color gradient represents point density, ranging from pale yellow (low density) to dark red (high density).

The spatial correspondence between forecast SSMI and GLEAM v4.2a observations is visualized in Figures. 7 and 8. All six architectures effectively reconstituted the broad latitudinal moisture deficiency gradient, precisely delineating high-intensity drought nuclei in the southern lowlands of Gafsa and Sidi Bou Zid, moderate stress across the central Kairouan plains, and comparatively attenuated conditions in the Kasserine highlands. The primary divergence in predictive fidelity was localized in Siliana, where complex orographic precipitation inputs generated acute high-frequency SSMI gradients. The scatter probability density functions (Figure8) show that BPNN produced the tightest clustering along the 1:1 identity line during testing, while XGBoost maintained the narrowest residual spread during independent validation. All models displayed increased residual scatter within the extreme drought domain (SSMI ≤ −1.5), consistent with the limited frequency of such events in the training distribution.

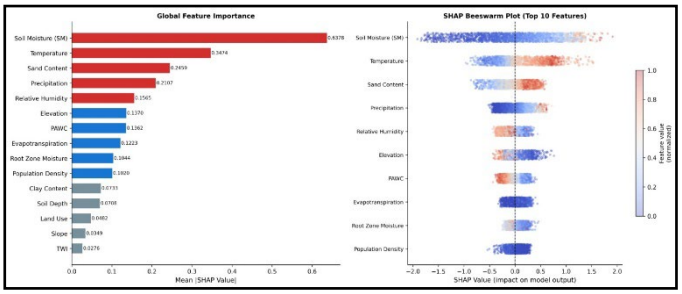

Figure 9: SHAP feature importance analysis for the XGBoost model (n = 2,000 test-set observations). (a) Global feature importance measured by mean absolute SHAP value ($|\varphi_i|$). Features are ranked from most (top) to least (bottom) important. Soil Moisture (SM) dominates with $|\varphi| = 0.638$ (26.0% of total contributions). (b) SHAP beeswarm plot for the top 10 features. Each point represents one observation; horizontal position indicates the SHAP value (impact on predicted SSMI); color indicates the normalized feature value (blue: low; red: high). The vertical dashed line at 0 separates drought-promoting (left) from wet-promoting (right) contributions.

4.3 TreeSHAP Feature Importance

4.3.1 Global Feature Importance

The TreeSHAP framework was applied to the XGBoost model using a representative sample of 2,000 test-set observations. Global feature importance, quantified via mean absolute SHAP values, is depicted in Figure9.

Surface soil moisture (SM) from NASA POWER MERRA-2 — an atmospheric reanalysis product entirely independent of the GLEAM v4.2a source used to compute the SSMI target — emerges as the dominant predictor (mean $|\varphi| = 0.638$; 26.0% of total contributions), confirming that the model exploits genuine hydrometeorological covariance rather than a

mathematical identity between predictor and target (Martens, 2017). Temperature (T2M) ranked second (mean |φ| = 0.347; 14.2%), sand content third (mean |φ| = 0.246; 10.0%), precipitation fourth (mean |φ| = 0.211; 8.6%), and relative humidity fifth (6.4%), followed by elevation (5.6%), PAWC (5.5%), evapotranspiration (5.0%), root zone moisture (4.3%), and population density (4.2%).

By thematic domain: meteorological variables 38.3%, surface soil moisture 26.0%, soil properties 21.4%, topographic features 8.1%, and socioeconomic factors 6.1%, confirming that hydrometeorological forcing dominates (combined 64.3%) while edaphic and topographic conditions provide a substantial modulating effect (29.5%).

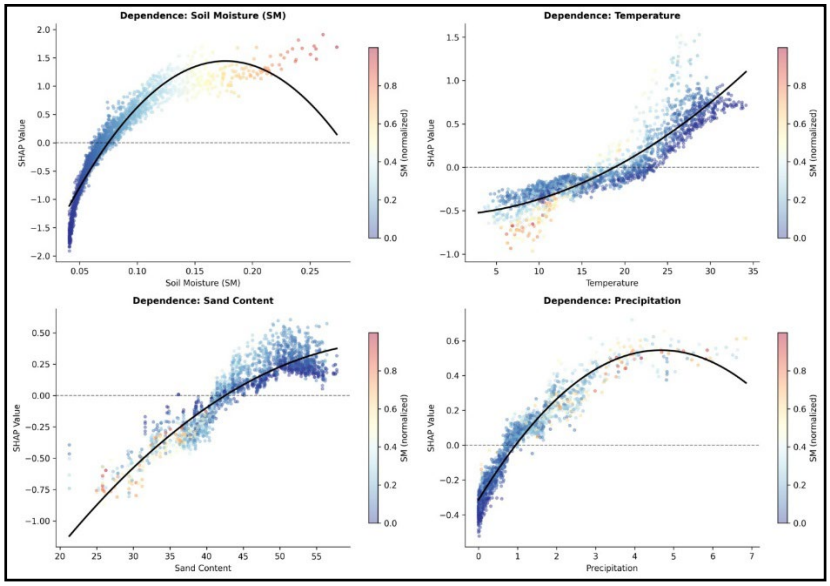

Figure 10: SHAP dependence plots for the four most important predictors (XGBoost model, n = 2,000 test-set observations). Each point represents one observation; the x-axis shows the feature value; the y-axis shows the corresponding SHAP value; point color represents normalized soil moisture (SM) value (blue: low SM; red: high SM). The solid black line shows a second-order polynomial trend. (a) Soil Moisture (SM, m^3 m^{-3}): near-linear positive relationship spanning SHAP values from −1.91 to +1.91. (b) Temperature (T2M, °C): sign-changing nonlinear effect; drought-promoting above 20 °C, neutral below 18 °C. (c) Sand Content (%): drought-amplifying effect intensifying with higher sand fractions. (d) Precipitation (PRECTOTCORR, mm day^{-1}): transition from drought-promoting to wet-promoting contributions at intermediate values.

4.3.2 Feature Effect Analysis

SHAP dependence plots for the top four predictors are presented in Figure10. For SM, SHAP values span the widest range (−1.91 to +1.91), with strongly positive contributions at high SM values and strongly negative contributions under low SM conditions. The total SHAP range for SM (3.82 units) approaches the full SSMI scale (−3 to +3). For temperature, SHAP values range from −0.96 to +1.53 with a positive mean (+0.019) and a strongly bimodal distribution: values become strongly negative when temperature exceeds 30 °C (summer, drought-promoting) and turn positive at high-elevation winter sites (humidity-promoting). For sand content, negative SHAP values are systematically associated with higher sand fractions. For precipitation, the SHAP transition from negative to positive occurs at intermediate levels, with the most negative contributions in pixels receiving less than 200 mm $year^{-1}$.

4.3.3 Spatiotemporal SHAP Maps

Spatiotemporal SHAP maps were computed by aggregating SHAP values by governorate and season. MERRA-2 SM SHAP values show the highest spatial variability, closely tracking soil moisture anomaly patterns: in Gafsa and Sidi Bou Zid, SM SHAP contributions are strongly negative during 2021–2022 drought months, while in Kasserine, SM SHAP values remain closer to neutral or slightly positive in autumn and winter. Temperature SHAP contributions exhibit a strong seasonal signal: summer months (June–August) show the most strongly negative values across all governorates, while winter months show weaker or positive contributions. The spatial distribution of soil property SHAP values (sand content, PAWC) reveals clusters of high agricultural drought vulnerability aligned with the sandy soils of Sidi Bou Zid and Gafsa.

5. Discussion

5.1 Model Ranking and Generalization under Climate Extremes

The overall performance ranking on the test set — BPNN > XGBoost > LightGBM > LSTM > CatBoost > RF — presents a nuanced picture that challenges the prevailing consensus in tabular environmental modelling (Grinsztajn, 2022). The BPNN advantage is best understood as a feature-space effect rather than a general architectural superiority: the inclusion of MERRA-2 surface SM as a predictor effectively recasts the prediction task from a complex multi-source regression to one with a dominant near-linear component, which BPNN's smooth, continuous activation functions approximate with high fidelity. Gradient boosting models, by contrast, rely on piecewise-constant tree splits that introduce quantization error in representing this near-linear SM–SSMI relationship. This interpretation is corroborated by the TreeSHAP analysis, which identifies SM as the dominant predictor (26.0% of total contributions) with a SHAP range (−1.91 to +1.91) effectively spanning the full SSMI scale.

On the independent validation set (2021–2022), the performance ranking partially reverses: XGBoost records the highest accuracy while BPNN drops to third position. This crossover indicates that BPNN's superior test-set performance partially reflects fitting to the specific temporal patterns of the 2015–2020 period, whereas XGBoost's robustness during the unprecedented 2021–2022 drought episode points to stronger extrapolation capacity. With a mean SSMI of −0.406 and 48.8% of observations falling within drought categories, the 2021–2022 episode represents a substantial distributional shift relative to the training period, constituting a stringent test of model generalization under climate extremes. This finding demonstrates that model evaluation for operational drought monitoring must systematically include independent validation on extreme drought periods, as standard test-set rankings may not reflect real-world behavior under distributional shift.

5.2 Physical Interpretation of SHAP Results

The SHAP summary distribution in figure 9 characterizes the influence of the 15 predictors on the XGBoost model output. Features are ranked vertically by global importance, with the chromatic scale representing feature magnitude (warm for elevated values; cool for diminished values) and horizontal displacement denoting the SHAP value. Positive coordinates correspond to higher SSMI (moisture surplus), whereas negative coordinates indicate drought-promoting contributions.

Surface SM dominates the plot in figure 9 with a SHAP range far exceeding any other feature (as quantified in Section 4). This near-linear monotonic relationship confirms that MERRA-2 SM alone can shift the model prediction from humid to extreme drought conditions, reflecting genuine hydrometeorological covariance rather than a mathematical identity between predictor and target — consistent with the strong but imperfect cross-source correlation already documented in the feature importance analysis.

The comparatively lower ranking of precipitation relative to SM — which runs counter to a priori expectations in semi-arid climates — is explained by the temporal aggregation structure of the dataset: at monthly timescales, SM already integrates precipitation variability from the current and preceding months, functioning as a memory variable that subsumes the direct precipitation signal.

Temperature exhibits an intermediate SHAP spread (−0.96 to +1.53) with a complex bimodal pattern: summer heat amplification is drought-promoting while winter temperature modulation is neutral to positive. Sand content displays a consistent negative association with SSMI, confirming the drought-amplifying effect of low water retention in coarse-textured soils. Precipitation SHAP values are concentrated in the range −0.52 to +0.72 with a mean near zero (−0.013), reflecting the variable, threshold-dependent nature of precipitation effects on monthly soil moisture.

The SM dependence plot shown in figure10 confirms a near-linear positive relationship across the full observed range (0.04–0.35 m^3 m^{-3}), with the steepest slope in the mid-range (SM = 0.06–0.15). This threshold behavior carries direct practical significance: it defines the critical soil moisture window within which on-farm interventions (supplementary irrigation, soil conservation measures) can most effectively shift SSMI from drought to near-normal categories. For temperature, the sign-changing nonlinear relationship confirms the contrasting roles of cool winters (drought-mitigating, below 18 °C) and hot summers (drought-amplifying, above 20 °C) across the five governorates.

5.3 Spatiotemporal Drought Vulnerability and Edaphic Controls

The spatiotemporal SHAP analysis reveals marked spatial heterogeneity in drought-controlling mechanisms not captured by global importance metrics (Abbes, 2023; Mardian, 2023). In Gafsa and Sidi Bou Zid, SM and precipitation SHAP contributions are strongly and persistently negative throughout the year, reflecting chronic moisture deficits driven by the combination of low annual precipitation (~188 mm), high temperatures (>20 °C), and sandy soils with low water retention capacity. These governorates represent areas of structurally elevated agricultural drought vulnerability where smart early-warning systems and precision irrigation interventions are most urgently needed.

In Kasserine and Siliana, SM SHAP values fluctuate seasonally, with partial positive contributions in winter linked to precipitation recovery from westerly weather systems interacting with Jebel Chambi topography. The anomalous model performance in Siliana (XGBoost: R^2 = −0.221) is attributable to this orographic precipitation dynamic: localized moisture inputs from the Jebel Chambi massif generated abrupt SSMI fluctuations deviating from the regional drought pattern encountered during training, exposing the limitations of tree-based architectures in topographically complex semi-arid settings. Neural network architectures (BPNN, LSTM) demonstrated a clear advantage in this context, reinforcing their utility for simulating nonlinear temporal dynamics under atypical climatic stress.

Sand content SHAP maps reveal spatially persistent negative contributions concentrated in the sandy plains of Sidi Bou Zid and Gafsa, where sand fractions exceed 50% and PAWC values are at their lowest. This edaphic signal is independent of the meteorological forcing and represents a structural amplifier of drought severity that cannot be mitigated by precipitation alone, pointing to the importance of soil amendment programs and cover crop strategies as complementary drought adaptation measures.

5.4 Comparative Evaluation of Machine Learning Architectures

The strong performance of LSTM (R^2 = 0.790 on the test set, R^2 = 0.667 on the validation set) confirms the value of temporal memory architectures for agricultural drought prediction: LSTM's gating mechanisms capture multi-month soil moisture persistence and drought propagation dynamics partially missed by the static, single-time-step representation of the other models. This advantage is most evident in governorates with strong month-to-month SSMI autocorrelation, such as Kasserine and Sidi Bou Zid.

The performance gap between RF (R^2 = 0.681) and the remaining models is consistent with the known limitations of bagging-based ensembles on regression tasks involving extreme values: RF's averaging mechanism systematically attenuates predictions toward the mean, producing underestimation of severe drought conditions (SSMI ≤ −1.5) and overestimation of extreme wet conditions. This smoothing bias is particularly consequential for operational agricultural drought monitoring where accurate prediction of tail events is critical for timely on-farm decision-making.

XGBoost achieves the most favorable balance between test-set accuracy (second-highest R^2 = 0.817) and validation generalization (highest R^2 = 0.696), making it the recommended model for operational agricultural drought prediction in this study area. Its interpretability via TreeSHAP, combined with resistance to overfitting through L1/L2 regularization and subsampling, positions XGBoost as the most suitable candidate for integration into a smart decision-support system requiring regular updates with incoming observational data.

5.5 Implications for Smart Agricultural Drought Management

The spatially explicit, physically interpretable outputs generated by the XGBoost–TreeSHAP framework translate directly into actionable guidance for smart agricultural drought management. The identification of critical SM thresholds (SM = 0.06–0.15 m^3 m^{-3}) as the zone of maximum SHAP sensitivity provides a scientifically grounded trigger for precision irrigation scheduling: when MERRA-2 SM falls below this window, supplementary irrigation can most effectively prevent SSMI from crossing drought classification thresholds. The spatial targeting of Gafsa and Sidi Bou Zid as structurally vulnerable zones — driven by the combination of sandy soils, low PAWC, and high temperatures — provides a quantitative basis for prioritizing drought resilience investments, including drip irrigation infrastructure, soil organic matter enhancement programs, and drought-tolerant crop variety deployment.

At the regional scale, the governorate-level SHAP disaggregation enables differentiated early-warning trigger calibration: thresholds derived from the Gafsa SHAP distributions differ meaningfully from those applicable to Kasserine or Siliana, reflecting the contrasting edaphic and topographic controls on drought propagation. Embedding this framework within an operational pipeline fed by near-real-time MERRA-2 and GLEAM data streams would enable monthly drought forecasting with actionable spatial resolution, directly supporting agricultural extension services, water allocation decisions, and insurance assessment for smallholder farmers across semi-arid Tunisia.

5.6 Perspectives and Future Directions

The integrated framework developed here is designed for broad transferability: by substituting region-specific feature datasets, it can be extended to other semi-arid territories of North Africa and the wider Mediterranean basin (Morocco, Algeria, Libya, Egypt), supplying spatially explicit drought early-warning information to support smart agricultural water management across the Maghreb region.

Several avenues for future research merit attention. First, incorporating near-real-time satellite soil moisture products (SMOS, Sentinel-1 SAR) and updated NASA POWER data into the prediction pipeline would enable operational monthly drought forecasting with a one-to-two-month lead time, providing actionable early-warning information to agricultural extension services and water resource managers (Koppa, 2022). Second, the spatiotemporal SHAP framework could be refined by disaggregating results to sub-governorate administrative units (délégations) and adopting crop-calendar-aware seasonal windows (pre-sowing, growing, and harvest seasons), enhancing the agricultural relevance of drought risk maps. Combining SHAP interpretation with multi-model ensemble approaches could additionally quantify how model uncertainty propagates into prediction variability (Covert, 2020; Fryer, 2021). Third, future investigations should examine the direct integration of SHAP values into adaptive model updating procedures: SHAP-guided feature selection could identify predictors contributing most to performance degradation during unprecedented drought episodes, enabling dynamic model recalibration as new observations accumulate. Finally, the anomalous performance breakdown in Siliana points to the need for finer-scale topographic datasets and sub-0.05° soil moisture products, potentially incorporating topographically downscaled precipitation fields from RegCM or WRF regional climate models.

6. Conclusion

This study developed and validated a robust, interpretable machine learning framework for agricultural drought prediction across five semi-arid governorates of central Tunisia during 2001–2022, integrating multi-source satellite and reanalysis datasets with six machine learning architectures and TreeSHAP explainability analysis. Four principal findings emerge from this work.

First, the performance evaluation reveals an unexpected model ranking in which BPNN outperforms all gradient boosting algorithms on the test set, attributable to the near-linear SM–SSMI relationship that smooth activation functions capture more precisely than piecewise-constant tree splits. On the independent extreme validation period, however, XGBoost demonstrates superior generalization, establishing it as the most robust architecture for operational drought prediction under distributional shift. This crossover underscores the necessity of including extreme-period validation in any model selection procedure for climate applications.

Second, TreeSHAP interpretability analysis identifies MERRA-2 surface soil moisture as the dominant agricultural drought predictor, followed by temperature, sand content, and precipitation, with hydrometeorological forcing (64.3%) modulated by edaphic and topographic conditions (29.5%). This hierarchy confirms that soil texture is a non-negligible

structural amplifier of drought severity that must be incorporated in regional monitoring frameworks.

Third, spatiotemporal SHAP disaggregation reveals that Gafsa and Sidi Bou Zid are the most structurally vulnerable governorates, driven by the compounding effects of chronic moisture deficits, high temperatures, and sandy soils with low water retention capacity. Siliana exhibits anomalous dynamics linked to orographic precipitation from the Jebel Chambi massif, highlighting the limits of tree-based models in topographically complex settings and the advantage of neural network architectures in such contexts.

Fourth, the spatially explicit, physically grounded SHAP outputs translate directly into actionable guidance for smart agricultural management, including precision irrigation trigger calibration, spatial prioritization of drought resilience investments, and differentiated early-warning threshold setting across governorates. Embedding this framework within operational systems fed by continuous satellite data streams can provide spatially targeted decision-support for drought early-warning and water resource allocation across semi-arid agricultural regions of North Africa and the Mediterranean basin.

Author Contributions

Conceptualization, K.M. and M.A.; methodology, K.M.; validation, M.A. and K.M.; formal analysis, M.A.; investigation, M.A.; resources, K.M.; data curation, M.A.; writing — original draft preparation, M.A.; writing — review and editing, M.A.; visualization, K.M.; supervision, K.M.; project administration, K.M. All authors have read and agreed to the published version of the manuscript.

Funding

The authors gratefully acknowledge financial support from the Deanship of Scientific Research, King Faisal University (KFU), Saudi Arabia. Grant number KFU261930.

Data Availability Statement

The datasets generated and analyzed for this study can be found in the Zenodo repository at https://doi.org/10.5281/zenodo.18733246. The complete Python code for data processing, machine learning model training, and SHAP interpretability analysis is publicly available on GitHub at https://github.com/ARGOUBI25/drought-prediction-tunisia.

Acknowledgments

The authors express their gratitude to King Faisal University and the University of Sousse for providing a conducive academic environment and essential resources. Special thanks are extended to the technical teams and organizations involved in maintaining the global datasets (GLEAM, NASA POWER, ISRIC, and ESA) used in this study, whose contributions were vital to its completion.

Declaration Of Competing Interest

The authors declare that the research was conducted in the absence of any commercial or financial relationships that could be construed as a potential conflict of interest.

Declaration Of Generative Ai And Ai-assisted Technologies

During the preparation of this work, the authors used Claude (Anthropic) to assist with language editing, manuscript structure refinement, and LaTeX formatting. After using this tool, the authors reviewed and edited all content as needed and take full responsibility for the scientific accuracy and integrity of the published article.

References

Abadi, M., Agarwal, A., Barham, P., Brevdo, E., Chen, Z., Citro, C., Corrado, G. S., Davis, A., Dean, J., Devin, M., et al., 2016. TensorFlow: Large-scale machine learning on heterogeneous distributed systems. arXiv:1603.04467.

Abbes, A. B., Inoubli, R., Rhif, M., and Farah, I., 2023. Combining deep learning methods and multi-resolution analysis for drought forecasting modeling. Earth Science Informatics. https://doi.org/10.1007/s12145-023-01009-4.

AghaKouchak, A., 2014. A baseline probabilistic drought forecasting framework using standardized soil moisture index: Application to the 2012 United States drought. Hydrology and Earth System Sciences, 18, 2485–2502. https://doi.org/10.5194/hess-18-2485-2014.

AghaKouchak, A., Huning, L. S., Sadegh, M., Qin, Y., Markonis, Y., Vahedifard, F., Love, C. A., Mishra, A., Mehran, A., Obringer, R., et al., 2023. Toward impact-based monitoring of drought and its cascading hazards. Nature Reviews Earth and Environment, 4, 582–595. https://doi.org/10.1038/s43017-023-00457-2.

Bahri, H., Annabi, M., M'Hamed, H. C., and Frija, A., 2022. Mapping soil organic carbon stocks in Tunisian topsoils. Data in Brief, 42, 108081. https://doi.org/10.1016/j.dib.2022.108081.

Bazza, M., Kay, M., and Knutson, C., 2018. Drought characteristics and management in North Africa and the Near East. FAO Water Reports, 45.

Beven, K. J., and Kirkby, M. J., 1979. A physically based, variable contributing area model of basin hydrology. Hydrological Sciences Bulletin, 24, 43–69. https://doi.org/10.1080/02626667909491834.

Borselli, L., and Torri, D., 2010. Soil roughness, slope and surface storage relationship for impervious areas. Journal of Hydrology, 393, Pp. 213–226. https://doi.org/10.1016/j.jhydrol.2010.08.013.

Breiman, L., 2001. Random forests. Machine Learning, 45, Pp. 5–32. https://doi.org/10.1023/A:1010933404324

Chen, T., and Guestrin, C., 2016. XGBoost: A scalable tree boosting system. In Proceedings of the 22nd ACM SIGKDD International Conference on Knowledge Discovery and Data Mining (pp. 785–794). ACM. https://doi.org/10.1145/2939672.2939785.

Chenoweth, J., Hadjinicolaou, P., Bruggeman, A., Lelieveld, J., Levin, Z., Lange, M. A., Xoplaki, E., and Hadjikakou, M., 2011. Impact of climate change on the water resources of the eastern Mediterranean and Middle East region: Modeled 21st century changes and implications. Water Resources Research, 47, W06506. https://doi.org/10.1029/2010WR010269.

Chollet, F., et al., 2018. Keras. https://keras.io.

Choubin, B., Borji, M., Mosavi, A., Dineva, K., et al., 2020. An ensemble hybrid machine learning model for drought prediction using SPI and SPEI indices. Water, 12, 3441. https://doi.org/10.3390/w12123441.

Covert, I., and Lee, S.-I., 2020. Improving interpretability of deep learning models with feature attribution. arXiv:2006.05689.

Dikshit, A., Pradhan, B., and Alamri, A. M., 2021. An improved SPEI drought forecasting approach using the long short-term memory neural network. Journal of Environmental Management, 283, 111979. https://doi.org/10.1016/j.jenvman.2021.111979.

Ding, Y., Xu, J., Wang, X., Cai, H., Zhou, Z., Han, S., and Hu, X., 2021. Propagation of meteorological to soil moisture drought: Influence of climate variables and socioeconomic factors. Journal of Hydrology, 603, 127014. https://doi.org/10.1016/j.jhydrol.2021.127014

Ekmekcioglu, O., et al., 2023. Drought forecasting using integrated variational mode decomposition and extreme gradient boosting. Water, 15, 3413. https://doi.org/10.3390/w15193413.

Elmotawakkil, A., et al., 2025. Machine learning techniques for soil moisture prediction in arid and semi-arid regions: A case study of Morocco. Intelligent Geoengineering, 2, Pp. 251–261. https://doi.org/10.1016/j.ige.2025.11.001.

Fitton, N., Alexander, P., Arnell, N., Bajzelj, B., Calvin, K., Doelman, J., Gerber, J. S., Havlik, P., et al., 2019. The vulnerabilities of agricultural land and food production to future water scarcity. Global Environmental Change, 58, 101936. https://doi.org/10.1016/j.gloenvcha.2019.101936.

Food and Agriculture Organization of the United Nations., 2020. AQUASTAT country profile – Tunisia. FAO. https://www.fao.org/aquastat/en/countries-and-basins/country-profiles/country/TUN.

Food and Agriculture Organization of the United Nations., 2022. Tunisia – Drought country case study: Vulnerability and impact assessment. https://www.fao.org/in-action/drought-portal/preparedness/vulnerability-and-impact-assessment/national-case-studies/tunisia/en.

Francis, D., Fonseca, R., Nelli, M., Temimi, M., Weston, M., Shen, Y., Abida, R., Almazroui, M., Al-Yahyai, S., Attada, R., et al., 2024. Recent and

projected changes in climate patterns in the Middle East and North Africa (MENA) region. Scientific Reports, 14, 60976. https://doi.org/10.1038/s41598-024-60976-w.

Fryer, K., et al., 2021. Interpretable machine learning for water quality prediction: A case study. Water Research, 198, 117153. https://doi.org/10.1016/j.watres.2021.117153.

Gorelick, N., Hancher, M., Dixon, M., Ilyushchenko, S., Thau, D., and Moore, R., 2017. Google Earth Engine: Planetary-scale geospatial analysis for everyone. Remote Sensing of Environment, 202, 18–27. https://doi.org/10.1016/j.rse.2017.06.031.

Gorokhovich, Y., and Voustianious, A., 2006. Accuracy assessment of the processed SRTM-based elevation data by CGIAR using field data from USA and Thailand and its relation to the terrain characteristics. Remote Sensing of Environment, 104, 409–415. https://doi.org/10.1016/j.rse.2006.05.012.

Grinsztajn, L., Oyallon, E., and Varoquaux, G., 2022. Why do tree-based models still outperform deep learning on tabular data? In Advances in Neural Information Processing Systems 35 (NeurIPS) Pp. 5079–5092.

Guo, Z. Q., et al., 2022. Soil texture is an important factor determining how microplastics affect soil hydraulic characteristics. Environment International, 164, 107253. https://doi.org/10.1016/j.envint.2022.107253.

Hao, Z., and AghaKouchak, A., 2013. Multivariate standardized drought index: A parametric multi-index model. Advances in Water Resources, 57, Pp. 12–18. https://doi.org/10.1016/j.advwatres.2013.03.009.

Hochreiter, S., and Schmidhuber, J., 1997. Long short-term memory. Neural Computation, 9, 1735–1780. https://doi.org/10.1162/neco.1997.9.8.1735.

Hulsman, P., Keune, J., Koppa, A., Schellekens, J., and Miralles, D. G., 2023. Incorporating plant access to groundwater in existing global, satellite-based evaporation estimates. Water Resources Research, 59. https://doi.org/10.1029/2022WR033731.

Jabro, J. D., Iversen, W. M., Stevens, W. B., and Evans, R. G., 2008. In-situ soil-water retention and field water capacity measurements in two contrasting soil textures. In Proceedings of the ASABE Annual International Meeting.

Ke, G., Meng, Q., Finley, T., Wang, T., Chen, W., Ma, W., Ye, Q., and Liu, T.-Y., 2017. LightGBM: A highly efficient gradient boosting decision tree. In Advances in Neural Information Processing Systems Vol. 30, Pp. 3146–3154.

Koppa, A., Rains, D., Hulsman, P., Poyatos, R., and Miralles, D. G., 2022. A deep learning-based hybrid model of global terrestrial evaporation. Nature Communications, 13, 1912. https://doi.org/10.1038/s41467-022-29543-7.

Li, J., Zhang, S., Huang, L., Zhang, T., and Feng, P., 2020. Drought prediction models driven by meteorological and remote sensing data in Guanzhong Area, China. Hydrology Research, 51, Pp. 942–958. https://doi.org/10.2166/nh.2020.184.

Li, J., et al., 2021. Robust meteorological drought prediction using antecedent SST fluctuations and machine learning. Water Resources Research. https://doi.org/10.1029/2020WR029413.

Liu, Y., et al., 2022. Influence of different meteorological factors on the accuracy of back propagation neural network simulation of soil moisture in China. Sustainability, 14, 16381. https://doi.org/10.3390/su142416381.

Lloyd, C. T., Sorichetta, A., and Tatem, A. J., 2017. High resolution global gridded data for use in population studies. Scientific Data, 4, 170001. https://doi.org/10.1038/sdata.2017.1.

Lotfirad, M., Esmaeili-Gisavandani, H., and Adib, A., 2022. Drought monitoring and prediction using SPI, SPEI, and random forest model in various climates of Iran. Journal of Water and Climate Change, 13, Pp. 383–406. https://doi.org/10.2166/wcc.2021.287.

Lundberg, S. M., Erion, G., Chen, H., DeGrave, A., Prutkin, J. M., Nair, B., Katz, R., Himmelfarb, J., Bansal, N., and Lee, S.-I. Pp. 2020. From local explanations to global understanding with explainable AI for trees. Nature Machine Intelligence, 2, 56–67. https://doi.org/10.1038/s42256-019-0138-9.

Lundberg, S. M., and Lee, S.-I., 2017. A unified approach to interpreting model predictions. In Advances in Neural Information Processing Systems 30 (NeurIPS) Pp. 4765–4774. https://doi.org/10.48550/arXiv.1705.07874.

Mardian, J., et al., 2023. A machine learning framework for predicting and understanding the Canadian Drought Monitor. Water Resources Research, 59. https://doi.org/10.1029/2022WR033847.

Martens, B., Miralles, D. G., Lievens, H., van der Schalie, R., de Jeu, R. A. M., Fernández-Prieto, D., Beck, H. E., Dorigo, W. A., and Verhoest, N. E. C., 2017. GLEAM v3: Satellite-based land evaporation and root-zone soil moisture. Geoscientific Model Development, 10, Pp. 1903–1925. https://doi.org/10.5194/gmd-10-1903-2017.

McKee, T. B., Doesken, N. J., and Kleist, J., 1993. The relationship of drought frequency and duration to time scales. In Preprints, 8th Conference on Applied Climatology Pp. 79–183. American Meteorological Society.

Ministère de l'Agriculture, des Ressources Hydrauliques et de la Pêche (MARHP)., 2022. Rapport national du secteur de l'eau – Année 2021 (mis à jour 2022). Bureau de la Planification et des Équilibres Hydrauliques. http://www.onagri.tn/uploads/secteur-eau/RNE_2021_V-Anglaise.pdf.

Ministère de l'Agriculture, des Ressources Hydrauliques et de la Pêche (MARHP)., 2023. Rapport national du secteur de l'eau – Année 2023. Bureau de la Planification et des Équilibres Hydrauliques. http://www.onagri.nat.tn/uploads/secteur-eau/eau-2023-anglais.pdf.

Miralles, D. G., Bonte, O., Koppa, A., Baez-Villanueva, O. M., Tronquo, E., Zhong, F., Beck, H. E., Hulsman, P., Dorigo, W. A., Verhoest, N. E. C., et al., 2025. GLEAM4: Global land evaporation and soil moisture dataset at 0.1° resolution from 1980 to near present. Scientific Data, 12, 416. https://doi.org/10.1038/s41597-025-04610-y.

Miralles, D. G., Holmes, T. R. H., de Jeu, R. A. M., Gash, J. H., Meesters, A. G. C. A., and Dolman, A. J., 2011. Global land-surface evaporation estimated from satellite-based observations. Hydrology and Earth System Sciences, 15, 453–469. https://doi.org/10.5194/hess-15-453-2011.

Molnar, C., 2025. Interpretable machine learning: A guide for making black box models explainable (3rd ed.). https://christophm.github.io/interpretable-ml-book.

Moriasi, D. N., Arnold, J. G., Van Liew, M. W., Bingner, R. L., Harmel, R. D., and Veith, T. L. , 2007. Model evaluation guidelines for systematic quantification of accuracy in watershed simulations. Transactions of the ASABE, 50, 885–900. https://doi.org/10.13031/2013.23153.

Muñoz-Sabater, J., Dutra, E., Agustí-Panareda, A., Albergel, C., Arduini, G., Balsamo, G., Boussetta, S., Brown, M., Buizza, R., et al., 2021. ERA5-Land: A state-of-the-art global reanalysis dataset for land applications. Earth System Science Data, 13, 4349–4383. https://doi.org/10.5194/essd-13-4349-2021.

Nadal-Romero, E., et al., 2025. Plant cover determines runoff generation in response to dry and wet conditions. Journal of Hydrology. https://doi.org/10.1016/j.jhydrol.2025.133495.

Observatoire National de l'Agriculture (ONAGRI)., 2023. Rapport annuel sur le secteur de l'eau et situation hydrique 2023. Ministère de l'Agriculture.

Osman, A. I. A., et al., 2025. A review on machine learning models for drought monitoring and forecasting. Environmental and Sustainability Indicators. https://doi.org/10.1016/j.indic.2025.100072.

Ouassanouan, Y., Simonneaux, V., Kharrou, M. H., et al., 2025. Downscaled ERA5 Land addresses agrometeorological data scarcity in North African basins. Scientific Reports, 15, 38533. https://doi.org/10.1038/s41598-025-20552-2.

Palagiri, H., et al., 2024. Parametric and non-parametric indices for agricultural drought assessment using ESACCI soil moisture data over the Southern Plateau and Hills, India. International Journal of Applied Earth Observation and Geoinformation. https://doi.org/10.1016/j.jag.2024.104531.

Pedregosa, F., Varoquaux, G., Gramfort, A., Michel, V., Thirion, B., Grisel, O., Blondel, M., Prettenhofer, P., Weiss, R., Dubourg, V., et al., 2011. Scikit-learn: Machine learning in Python. Journal of Machine Learning Research, 12, 2825–2830.

Poggio, L., de Sousa, L. M., Batjes, N. H., Heuvelink, G. B. M., Kempen, B.,

Ribeiro, E., and Rossiter, D., 2021. SoilGrids 2.0: Producing soil information for the globe with quantified spatial uncertainty. SOIL, 7, 217–240. https://doi.org/10.5194/soil-7-217-2021.

Pokhrel, Y., Felfelani, F., Satoh, Y., Boulange, J., Burek, P., Gädeke, A., Gerten, D., Gosling, S. N., Grillakis, M., Gudmundsson, L., et al., 2021. Global terrestrial water storage and drought severity under climate change. Nature Climate Change, 11, 226–233. https://doi.org/10.1038/s41558-020-00972-w.

Prokhorenkova, L., Gusev, G., Vorobev, A., Dorogush, A. V., and Gulin, A., 2018. CatBoost: Unbiased boosting with categorical features. arXiv:1706.09516.

Purinton, B., and Bookhagen, B., 2021. Beyond vertical point accuracy: Assessing inter-pixel consistency in 30 m global DEMs for the arid Central Andes. Frontiers in Earth Science, 9, 758606. https://doi.org/10.3389/feart.2021.758606.

Rahmati, O., Falah, F., Naghibi, S. A., Biggs, T., Soltani, M., Deo, R. C., Cerdà, A., Mohammadi, F., and Tien Bui, D., 2019. Land subsidence modelling using tree-based machine learning algorithms. Science of the Total Environment, 672, 239–252. https://doi.org/10.1016/j.scitotenv.2019.03.496.

Ries, F., Schmidt, S., Sauter, M., and Lange, J., 2017. Controls on runoff generation along a steep climatic gradient in the Eastern Mediterranean. Journal of Hydrology: Regional Studies, 9, 18–33. https://doi.org/10.1016/j.ejrh.2016.12.001.

Roberts, D. R., Bahn, V., Ciuti, S., Boyce, M. S., Elith, J., Guillera-Arroita, G., Hauenstein, S., Lahoz-Monfort, J. J., Schröder, B., Thuiller, W., et al., 2017. Cross-validation strategies for data with temporal, spatial, hierarchical, or phylogenetic structure. Ecography, 40, 913–929. https://doi.org/10.1111/ecog.02881.

Romano, N., Nasta, P., Adamo, G., Bonfante, A., Chirico, G. B., Coppola, A., Comegna, A., Damiano, N., De Mascellis, R., Di Fusco, S., et al., 2022. Available water capacity from a multidisciplinary and multiscale viewpoint: A review. Agronomy for Sustainable Development, 42, 77. https://doi.org/10.1007/s13593-022-00774-8.

Saxton, K. E., and Rawls, W. J., 2006. Soil water characteristic estimates by texture and organic matter for hydrologic solutions. Soil Science Society of America Journal, 70, Pp. 1569–1578. https://doi.org/10.2136/sssaj2005.0117.

Sørensen, R., Zinko, U., and Seibert, J., 2006. On the calculation of the topographic wetness index: Evaluation of different methods based on field observations. Hydrology and Earth System Sciences, 10, 101–112. https://doi.org/10.5194/hess-10-101-2006.

Strohbach, M. W., Döring, A. O., Möck, M., Sedrez, M., Mumm, O., and Schneider, A.-K., 2019. The "hidden urbanization": Trends of impervious surface in low-density housing developments and resulting impacts on the water balance. Frontiers in Environmental Science, 7, 29. https://doi.org/10.3389/fenvs.2019.00029.

Sun, X., et al., 2022. Monitoring of extreme agricultural drought of the past 20 years in Southwest China using GLDAS soil moisture. Remote Sensing, 14, 1323. https://doi.org/10.3390/rs14061323.

Tanriverdi, I., et al., 2025. AI-driven U.S. drought prediction using machine learning and deep learning. Climate Dynamics. https://doi.org/10.1007/s00382-025-07720-w.

Tejedor, E., de Luis, M., Cuadrat, J. M., and Saz, M. Á., 2016. Tree-ring-based drought reconstruction in the Iberian Range (east of Spain) since 1694. International Journal of Biometeorology, 60, 361–372. https://doi.org/10.1007/s00484-015-1033-7.

Tejedor, E., Saz, M. Á., Esper, J., Cuadrat, J. M., and de Luis, M., 2017. Summer drought reconstruction in northeastern Spain inferred from a tree ring latewood network since 1734. Geophysical Research Letters, 44, 8492–8500. https://doi.org/10.1002/2017GL074748.

Tramblay, Y., Koutroulis, A., Samaniego, L., Vicente-Serrano, S. M., Volaire, F., Boone, A., Le Page, M., Llasat, M. C., Albergel, C., Burak, S., et al., 2020. Challenges for drought assessment in the Mediterranean region under future climate scenarios. Earth-Science Reviews, 210, 103348. https://doi.org/10.1016/j.earscirev.2020.103348.

Verner, D., Tréguer, D., Redwood, J., Christensen, J., McDonnell, R., Elbert, C., and Konishi, Y. , 2018. Climate variability, drought, and drought management in Tunisia's agricultural sector. World Bank. https://doi.org/10.1596/30604.

Vicente-Serrano, S. M., Beguería, S., and López-Moreno, J. I., 2010. A multiscalar drought index sensitive to global warming: The Standardized Precipitation Evapotranspiration Index. Journal of Climate, 23, Pp. 1696–1718. https://doi.org/10.1175/2009JCLI2909.1.

Xi, Y., Peng, S., Ciais, P., and Chen, Y., 2021. Future impacts of climate change on inland Ramsar wetlands. Nature Climate Change, 11, Pp. 45–51. https://doi.org/10.1038/s41558-020-00942-2.

Xu, P., et al., 2024. Comparative validation of recent 10 m-resolution global land cover maps. Remote Sensing of Environment. https://doi.org/10.1016/j.rse.2024.114334.

Zanaga, D., Van De Kerchove, R., Daems, D., De Keersmaecker, W., Brockmann, C., Kirches, G., Wevers, J., Cartus, O., Santoro, M., and Fritz, S., 2022. ESA WorldCover 10 m 2021 v200. https://doi.org/10.5281/zenodo.7254221.

Zellou, B., Rahali, B., et al., 2023. Review article: Towards improved drought prediction in the Mediterranean region – Modeling approaches and future directions. Natural Hazards and Earth System Sciences, 23, 3543–3565. https://doi.org/10.5194/nhess-23-3543-2023.

Zhang, B., et al., 2023. Explainable machine learning for the prediction and assessment of complex drought impacts. Science of the Total Environment, 898, 165509. https://doi.org/10.1016/j.scitotenv.2023.165509.

Zhang, Y., et al., 2021. Changes in soil water holding capacity and water availability following vegetation restoration on the Chinese Loess Plateau. Scientific Reports, 11, 90210. https://doi.org/10.1038/s41598-021-90210-1.